

Rapid Calibration of Operational and Research Meteorological Satellite Imagers. Part I: Evaluation of Research Satellite Visible Channels as References

PATRICK MINNIS AND LOUIS NGUYEN

Atmospheric Sciences, NASA Langley Research Center, Hampton, Virginia

DAVID R. DOELLING

Analytical Services and Materials, Inc., Hampton, Virginia

DAVID F. YOUNG

Atmospheric Sciences, NASA Langley Research Center, Hampton, Virginia

WALTER F. MILLER

Science Applications International Corporation, Hampton, Virginia

DAVID P. KRATZ

Atmospheric Sciences, NASA Langley Research Center, Hampton, Virginia

(Manuscript received 14 September 2001, in final form 11 March 2002)

ABSTRACT

Operational meteorological satellites generally lack reliable onboard calibration systems for solar-imaging channels. Current methods for calibrating these channels and for normalizing similar channels on contemporaneous satellite imagers typically rely on a poorly calibrated reference source. To establish a more reliable reference instrument for calibration normalization, this paper examines the use of research satellite imagers that maintain their solar-channel calibrations by using onboard diffuser systems that rely on the sun as an absolute reference. The Visible Infrared Scanner (VIRS) on the *Tropical Rainfall Measuring Mission (TRMM)* satellite and the second Along-Track Scanning Radiometer (ATSR-2) on the second *European Remote Sensing Satellite (ERS-2)* are correlated with matched data from the eighth *Geostationary Operational Environmental Satellite (GOES-8)*, the fifth *Geostationary Meteorological satellite (GMS-5)*, and with each other to examine trends in the solar channels. VIRS data are also correlated with the *Terra* satellite's Moderate Resolution Imaging Spectroradiometer (MODIS) provisional data as a preliminary assessment of their relative calibrations. As an additional check on their long-term stability, the VIRS data are compared to the relevant corresponding broadband shortwave radiances of the Clouds and the Earth's Radiant Energy System (CERES) scanners on *TRMM*. No statistically significant trend in the calibration of the VIRS 0.65- and 1.64- μm channels could be detected from the comparisons with CERES data taken during 1998 and 2000. The VIRS-to-GOES-8 correlations revealed an annual degradation rate for the GOES-8 visible (0.67 μm) channel of $\sim 7.5\%$ and an initial drop of 16% in the gain from the prelaunch value. The slopes in the GOES-8 visible-channel gain trend lines derived from VIRS data taken after January 1998 and ATSR-2 data taken between October 1995 and December 1999 differed by only 1%–2% indicating that both reference instruments are highly stable. The mean difference of 3%–4.8% between the VIRS–GOES-8 and ATSR-2–GOES-8 gains is attributed to spectral differences between ATSR-2 and VIRS and to possible biases in the ATSR-2 channel-2 calibration. A degradation rate of 1.3% per year found for the GMS-5 visible channel was confirmed by comparisons with earlier calibrations. The MODIS and VIRS calibrations agreed to within -1% to 3%. Some of the differences between VIRS and the provisional MODIS radiances can be explained by spectral differences between the two instruments. The MODIS measures greater reflectance than VIRS for bright scenes. Although both VIRS and ATSR-2 provide temporally stable calibrations, it is recommended that, at least until MODIS calibrations are finalized, VIRS should be used as a reference source for normalizing operational meteorological satellite imagers because of its broader visible filter.

1. Introduction

With the development of improved satellite imagers, faster computers, and more sophisticated algorithms, it

is possible to derive values for a host of scientific parameters over large areas in near real time from satellite data. The resulting datasets, including parameters such as top-of-atmosphere (TOA) radiation, cloud fraction, and cloud optical depth, are valuable for monitoring climate change and validating climate model results. In the future, they might benefit short-term weather fore-

Corresponding author address: Patrick Minnis, NASA Langley Research Center, MS 420, Hampton, VA 23681.
E-mail: p.minnis@larc.nasa.gov

casts. In either case, the products can be derived from a variety of satellites with imagers that have different spectral and calibration capabilities. To ensure consistency of results derived from the different sensors, it is essential to maintain stable cross calibrations. For applications requiring near-real-time results, it will be necessary to cross calibrate, in a timely manner, the various satellites with a reliable, known reference satellite. A systematic approach to effect such cross calibrations for many recent and historical satellites is described in this three-part paper. This paper, Part I, examines the stability and capability of research satellite imager visible channels for serving as references for operational satellites. Part II of this paper (Minnis et al. 2002) scrutinizes the differences in thermal channel temperatures for matched operational and research satellite imagers to determine if the infrared channels can be satisfactorily referenced to a single satellite. Finally, Part III of this paper (Nguyen et al. 2001, submitted to *J. Atmos. Oceanic Technol.*, hereafter NG01) develops the approach for monitoring and rapidly intercalibrating the various sensors. It also applies the visible-channel calibrations to a variety of historical satellite imagers to enhance their use in scientific studies and climate monitoring.

The utility of a satellite imager for scientific analysis necessitates a quantitative understanding of the sensor's accuracy either in a relative or absolute sense. In particular, long-term monitoring of climate variables requires an assessment of the temporal variation of the sensor accuracy. Most spectral imagers on operational meteorological satellites use onboard blackbody references to monitor and adjust the calibration coefficients for thermal infrared channels on a relatively frequent basis. The visible and near-infrared channels, however, have been less rigorously monitored, requiring the application of calibration updates using normalization to some reference data. These references include radiances from a comparable sensor calibrated on the surface and flown on a high-altitude aircraft (e.g., Abel et al. 1993), from internal measurements over a bright Earth target that is assumed to be constant over time (e.g., Rao and Chen 1996), from vicarious calibrations using measured or theoretical spectral surface albedos that are carefully adjusted to obtain TOA bidirectional reflectance (e.g., Kriebel and Amann 1993; Slater et al. 1996; Knapp and Vonder Haar 2000), or from other satellite instruments calibrated through one of the previous methods (Desormeaux et al. 1993; Minnis and Smith 1998). Although valuable and often used, these approaches are not entirely satisfactory because they introduce a variety of additional error sources such as mismatched fields of view, differences in spectral filters, changes in the reference target and overlying atmosphere, uncertainties in atmospheric profiles of relevant variables, a limited dynamic range, and the reliance on models to correct for anisotropy and the atmosphere. To minimize the impact of these external error sources, it is desirable to rely on

a more complete internal calibration system and stable reference source.

During the past 25 years, several research and operational satellite sensors have flown with onboard calibration systems for both solar and infrared channels. The broadband shortwave (SW; 0.3–5.0 μm) channels on the Earth Radiation Budget Experiment (ERBE; Barkstrom et al. 1990) were calibrated by viewing space to obtain a zero radiance and by viewing the sun via a diffuser plate to measure a stable radiance at the high end of the sensor's dynamic range. A similar technique is used to calibrate the Clouds and Earth's Radiant Energy System (CERES; Wielicki et al. 1998) SW channel on the *Tropical Rainfall Measuring Mission (TRMM)* and *Terra* satellites (Lee et al. 1998). Narrowband channel calibrations on the *ERS-2* Along Track Scanning Radiometer (ATSR-2; Mutlow et al. 1999), the *TRMM* Visible Infrared Scanner (VIRS; Barnes et al. 2000), and the *Terra* Moderate Resolution Imaging Spectroradiometer (MODIS; Butler and Barnes 1998) are also monitored and adjusted in this way. This approach eliminates most of the variables associated with the other techniques, leaving only the characterization of the diffuser as the main error source. To ensure that this technique was operating as expected for CERES, Priestley et al. (2000) examined the stability of the CERES calibrations on the *TRMM* at various times between 1998 and 2000. Continuous CERES data were taken by *TRMM* during the first 8 months and only sporadically between September 1998 and April 2000. Lyu et al. (2000) used the moon as reference to check the stability of the VIRS 0.65- and 1.6- μm channels during 1998, its first year of operation. Both studies showed no significant trends in any of the channels.

Because the diffuser approach applied to all of the aforementioned instruments uses the same reference sources, it follows that if each calibration system is operating correctly, the relative performance of the sensors should remain constant with time. Thus, by intercalibrating these various instruments, it should be possible to evaluate the relative long-term calibrations of one or more of the sensors. A quantitative evaluation of the relationships between similar channels on the ATSR-2 and VIRS also facilitates the use of those channels for remote sensing of the same quantities over the globe, but with complementary temporal and spatial coverage. Thus, combining results from the two sensors can be accomplished with minimal errors due to calibration differences.

Strong correlations exist between broadband SW and 0.65- μm radiances, respectively (e.g., Minnis and Harrison 1984; Minnis et al. 1995; Trishchenko and Li 1998; Doelling et al. 2001). Such correlations have been used to derive formulas for accurately estimating large-scale SW fluxes at the TOA when direct measurements of broadband radiation are unavailable (e.g., Minnis and Smith 1998; Doelling et al. 2001). Because of the strong correlations, any trends in the SW data should be mir-

rored in the corresponding narrowband channels depending on the temporal variations in the spectral characteristics of the viewed scenes. Highly accurate broadband data should therefore be useful for monitoring trends in narrowband data.

In this paper, VIRS spectral radiances are correlated to the corresponding channels of CERES and the ATSR-2 to examine the relative stability of their long-term calibrations over a period of 2–3 yr, beginning in January 1998. Additionally, the VIRS and ATSR-2 data are correlated with the relevant channels on the eighth *Geostationary Operational Environmental Satellite (GOES-8)* to determine if the relatively short record of VIRS can be used to predict the variation of the *GOES-8* calibration in the past thereby establishing VIRS as a longer-term calibration reference source. The visible (VIS; 0.65 μm) and near-infrared (NIR, 1.6 μm) channels are correlated with CERES SW data. Additionally, the VIS data are compared to their collocated counterparts measured by the ATSR-2. Young et al. (2001, submitted to *J. Atmos. Oceanic Technol.*, hereafter YM01) describe the comparisons of VIRS and ATSR-2 1.6- μm data. Preliminary intercalibrations between corresponding VIRS and MODIS channels are also included to ensure that these two well-calibrated instruments are consistent. Finally, the VIRS data are used to calibrate the VIS channel on the fifth *Geostationary Meteorological Satellite (GMS-5)* for 1 yr to facilitate use of those data in quantitative applications. The results of this study should be valuable for understanding the long-term stability of these important sensors and to further evaluate the relationship between narrowband and broadband radiances. They are also critical for determining the calibration of the other meteorological satellite imagers as shown in Part III (NG01).

2. Data

The *TRMM* satellite operates in a precessing orbit at 350 km above the Earth's surface with an inclination of 35°. Its sensors can observe at all local hours and available solar zenith angles (SZA) over a given location between roughly 37°N and 37°S during a 46-day period. *TRMM* was launched in November 1997 and all of the instruments became operational by 1 January 1998. The earth observing system *Terra* satellite was launched during December 1999 into a sun-synchronous orbit with a nominal equatorial crossing time of 1030 LT. *GOES-8* was launched 13 April 1994 and has been located at 75°W since September 1994. *GMS-5* was placed in operational service over the equator at 140°E during June 1995. The *ERS-2* was launched 21 July 1995 into a sun-synchronous orbit with a nominal equatorial crossing time of 1030 LT.

a. CERES

On *TRMM*, the CERES instrument has a nominal sub-satellite resolution of 10 km and scans to a nadir angle

of 90°. The scanner operates in both cross-track and rotating-azimuth plane modes. Only data taken in the former mode are used here. Lee et al. (1998) found that the calibrations of all three channels changed by less than $\pm 0.3\%$ from prelaunch to the initial on-orbit operations. Thomas et al. (2000) reported a 0% drift during the first 8 months of operation. The scanner was turned off during September 1998 and restarted for selective overpasses during 1999 and for the entire month of March 2000. Only the unfiltered radiances from 1998 and 2000 are used here. The uncertainty in the unfiltered SW (0.3–5 μm) radiance is 0.6%. Each CERES radiance is tagged with one of three surface types for this study. These include ocean, land, and desert as specified at a 2.5° resolution for ERBE (Barkstrom et al. 1990).

b. VIRS

The VIRS (Barnes et al. 2000) scans up to a viewing zenith angle (VZA) of $\theta = 48^\circ$ with a nominal subsatellite resolution of 2 km. The prelaunch and in-orbit calibration procedures and results for the first year of operation were reported by Barnes et al. (2000) and Lyu et al. (2000), respectively. Version-5 VIRS radiances are used here. The 1.6- μm radiances were adjusted for a filter leak at 5.2 μm , and then increased 17% as a result of comparisons with the ATSR-2, aircraft data, and theoretical calculations (YM01). For comparison with CERES, the VIRS data were convolved into collocated CERES footprints using the CERES point-spread function (Green and Wielicki 1995) to obtain a mean VIRS radiance L_{CV_x} for each CERES cross-track pixel out to $\theta = 48^\circ$. The subscripts CV and x refer to VIRS–CERES and the VIRS channel number, respectively. To compare with the ATSR-2 and *GOES-8* data, a mean VIS reflectance

$$\rho_{\text{V}_1} = \pi L_{\text{V}_1}(\theta_o, \theta, \phi) / E_v \mu_o \delta(D_y) \quad (1)$$

was computed using L_{V_1} , the mean VIRS channel-1 radiance for each box in a grid over the area of interest. The SZA and relative azimuth angle are θ_o and ϕ , respectively, μ_o is the $\cos\theta_o$, and δ is the Earth–sun distance correction factor computed for day of the year D_y . The nominal VIRS VIS solar constant E_v is 531.0 $\text{W m}^{-2} \text{sr}^{-1} \mu\text{m}^{-1}$ based on the spectral solar constant curve of Iqbal (1983). For comparisons with *GOES-8*, *GMS-5*, MODIS, and ATSR-2, the VIRS radiances are converted to equivalent *GOES-8* radiances by multiplying L_{V_1} by the ratio of the *GOES-8* and VIRS solar constants, $526.9 \text{ W m}^{-2} \text{sr}^{-1} \mu\text{m}^{-1} / E_v = 0.9923$. All of the data are averaged on a 0.5° grid for *GOES-8* and *GMS-5* and on a 0.25° grid for ATSR-2 and MODIS.

c. GOES-8

The *GOES-8* 5-channel imager has a 1-km VIS channel ($\sim 0.62 \mu\text{m}$) with data taken every 15 min at 10-bit resolution (Menzel and Purdom 1994). The operational

calibration procedures for *GOES-8* are described by Weinreb et al. (1997). Simple averaging is used to degrade the VIS resolution to a 4-km resolution to match the other *GOES-8* imager channels. The channel-1 (VIS) radiance is

$$L_{G1} = g_G(C_G - C_{G_o}), \quad (2)$$

where the gain is g_G , C_G is the 10-bit observed count, and the space count C_{G_o} is nominally fixed at 30.6. The *GOES-8* reflectance ρ_G is computed with (1) using 526.9 $\text{W m}^{-2} \text{sr}^{-1} \mu\text{m}^{-1}$ as the solar constant E_o . It is a value that was initially used for calibrating *GOES-6* (Whitlock et al. 1994) and is used here as a common scaling factor. For matching with other satellites, the data are averaged on a 0.5° grid. The correlations with VIRS used only those collocated data that were matched to within ± 15 min. Furthermore, the VIS data were restricted to areas unaffected by sunglint and to times when the difference between the respective values of θ and ϕ from the two satellites was less than 15° . Oceanic areas with significant sunglint were estimated using the ocean bidirectional reflectance model of Minnis and Harrison (1984), which provides anisotropic correction factors χ as a function of viewing and illumination angles. For all values of θ_o , pixels with $\chi > 1.4$ and $\phi < 75^\circ$ were assumed to be affected by sunglint and rejected. Additionally, pixels with $\theta_o < 25^\circ$ and $\chi > 1.5$ for all values of ϕ were rejected. Except for some deep convective systems, all of the data were taken over ocean.

d. GMS-5

The *GMS-5* Visible Infrared Spin Scan Radiometer has four channels with a nominal resolution of 5 km (1.25-km VIS). Unlike its predecessors, the *GMS-5* VIS channel (channel 1) is relatively broad, covering wavelengths between 0.55 and 1.05 μm . *GMS* VIS radiance is proportional to the square of the 8-bit VIS count C_{GM} ,

$$L_{GMV} = g_{GM}(C_{GM}^2 - C_{GM_o}^2), \quad (3)$$

where g_{GM} is the *GMS-5* VIS gain and C_{GM_o} is the space count. Matching of the *GMS-5* and VIRS data follows the same procedures as those for *GOES-8*, except that ocean and land targets are gridded separately for the VIS-channel matching.

e. MODIS

MODIS, a 36-channel imager, began producing the first usable imagery during 18 March 2000. It scans to a VZA of $\sim 70^\circ$ providing a swath width of 2330 km. Only 1-km resolution MODIS MOD021KM provisional data (available online at <http://modis.gsfc.nasa.gov/data/index.html>) taken with the "B-side" electronic configuration during November 2000 and January and March 2001 were used here. The provisional MODIS data, created during 2001, were calibrated in the same fashion between 1 November 2000 and 15 June 2001. The pre-

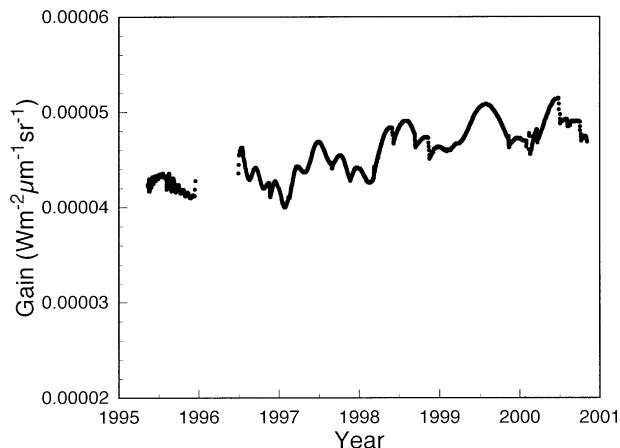


FIG. 1. Time series of ATSR-2 channel-2 gain.

launch calibration characteristics of the MODIS channels are discussed by Barnes et al. (1998). As of this writing, examination and validation of the MODIS dataset are continuing. MODIS channel 1 (0.645 μm), is correlated with the VIRS VIS channel. The MODIS VIS channel radiances L_M are also normalized using the ratio of the *GOES-8* solar constant to the MODIS channel-1 solar constant, $509.3 \text{ W m}^{-2} \text{sr}^{-1} \mu\text{m}^{-1}$. VIRS and MODIS data are matched in the same fashion as the *GOES-8*–VIRS data.

f. ATSR-2

The ATSR-2, a seven-channel radiometer on the *ERS-2*, produces a 555×512 image with a nominal resolution of 1 km. Calibration of the ATSR-2 solar channels is described by Smith et al. (1997). The ATSR-2 is a tilted conical scanner that create a series of images that provide views of a given area twice during an overpass: once near nadir and once at $\theta = 55^\circ$. Only the near-nadir view is used here. ATSR-2 data were selected if the subsatellite point was in the swath of the VIRS or *GOES-8* taken within 10 min of the *ERS-2* overpass. Only collocated data that matched to within $\pm 10^\circ$ of θ and ϕ were used in the correlations. The ATSR-2 visible-channel data are provided as normalized radiances r , the equivalent overhead-sun albedos at the nominal Earth–sun distance. The onboard calibrations (obtained from <http://www.atstr.rl.ac.uk/>) produced the variations in gain shown in Fig. 1 that are used to convert counts to reflectance. The changing Earth–sun distance gives rise to the annual cycle in gain with a superimposed seasonal cycle. The gradual increase in average gain is typical of degradation in the sensor optical components as a result of space exposure.

The ATSR-2 channel-2 GOES-equivalent VIS radiance was computed as

$$L_{A2} = rE_G/\mu_o \delta(D_y). \quad (4)$$

The ATSR-2 reflectance ρ_{A2} is equivalent to the ratio

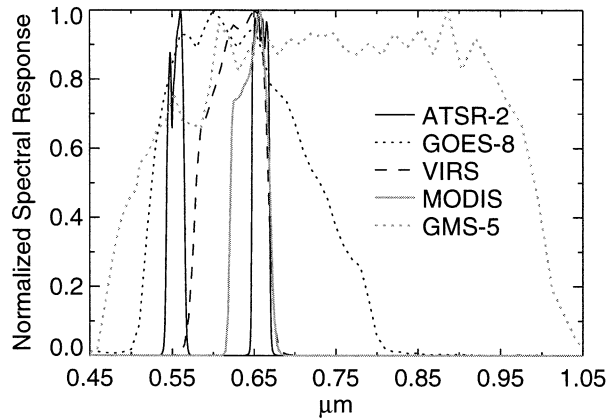


FIG. 2. Solar channel filter functions for ATSR-2, GOES-8, VIRS, MODIS, and GMS-5.

L_{A2}/E_G . The radiances for channel 2 ($0.67 \mu\text{m}$) were averaged on a 0.25° grid to minimize the effects of cloud movement. Most of the ATSR-2 data used for the VIRS comparisons were taken over ocean surfaces during two periods: February–August 1998 and February–July 2000. Some data were taken over the Amazon Basin during the 1998 period to obtain some optically thick clouds that increased the dynamic range. ATSR-2 data from selected months during 1995–99 were used in the GOES-8 comparisons.

g. Spectral summary

Figure 2 shows the spectral filter functions for the various VIS channels. The VIRS filter is relatively well centered within the GOES-8 filter while the ATSR-2 channel 2 is at longer wavelengths than the centers of the VIRS and GOES-8 filter functions. The MODIS VIS channel is about twice the width of the ATSR-2 channel and half that of VIRS. Like ATSR-2, it is centered at a longer wavelength than either VIRS or GOES-8. The GMS-5 VIS band includes all of the other bands as well as both shorter and longer wavelengths. Separate land and ocean calibrations are performed because GMS-5 VIS includes a broad segment of near-infrared wavelengths. The spectral differences seen in Fig. 2 are likely to result in some inherent biases between the various calibrated channels.

3. Methodology

a. CERES–VIRS

A linear fit between the VIRS and CERES radiances is computed for each hour of data. Because the relationship between narrowband and broadband solar reflectances varies with SZA (e.g., Minnis et al. 1995), the correlations between the CERES SW and the VIRS VIS and NIR data were computed for three ranges of SZA: 0° – 45° , 45° – 60° , and 60° – 90° . It is assumed that over the course of a year, the same sets of angles and

scenes over a given surface type will have been sampled sufficiently to eliminate any scene or angular dependence in the fits. Additionally, fits for each dataset from March 1998 and March 2000 are compared because they should, in effect, measure similar sets of angles and conditions.

The CERES SW radiances L_C are regressed against the corresponding VIRS radiances from channel i to obtain a linear equation

$$L_C = aL_{V1} + b. \quad (5)$$

Trends in the slopes a and offsets b are then computed for the entire time period along with statistical parameters to determine the significance of the resulting trends.

b. GOES-8–VIRS–ATSR-2

The visible channel data from the paired satellites are regressed using a least squares technique to obtain a value of g_G from GOES-8 and VIRS VIS data,

$$L_{G1} = L_{V1} = g_G(C_G - C_{G_o}), \quad (6)$$

and from ATSR-2 data,

$$L_{G1} = L_{A2} = g_G(C_G - C_{G_o}), \quad (7)$$

where the slope is g_G and the offset is the product $g_G C_{G_o}$. The matched VIRS and ATSR-2 reflectances were also regressed to obtain

$$\rho_{V1} = c\rho_{A2} + d, \quad (8)$$

where c and d are the slope and offset, respectively. Trend lines of slope and offset were computed for the VIRS–GOES-8 results.

c. VIRS–MODIS, VIRS–GMS-5

The VIRS and MODIS VIS data are correlated in the same fashion as in (8) except that the reflectances are replaced by the respective VIS and MODIS normalized radiances. For the GMS-5 VIS channel, the right side of (3) is regressed against L_{V1} . No trend lines are computed for the MODIS results because of the short period of available data.

4. CERES–VIRS results and discussion

Figure 3 shows the scatterplots and resulting fits for the VIRS VIS and CERES SW data taken over ocean areas between 2100 and 2200 UTC 12 January 1998. For $\theta_o < 45^\circ$ (Fig. 3a), the squared correlation coefficient R is 0.994 and the number of samples N is 47 889, while $a = 0.634 \mu\text{m}$ and $b = 8.84 \text{ W m}^{-2} \text{ sr}^{-1}$. The slope increases to $0.650 \mu\text{m}$ (Fig. 3b) and $0.683 \mu\text{m}$ (Fig. 3c) for $45^\circ \leq \theta_o < 60^\circ$ and $\theta_o \geq 60^\circ$, respectively, while the offsets decrease with θ_o . The correlation coefficients are roughly the same for all SZAs. Over land, the slopes are smaller by 1%–8%, but the intercepts are

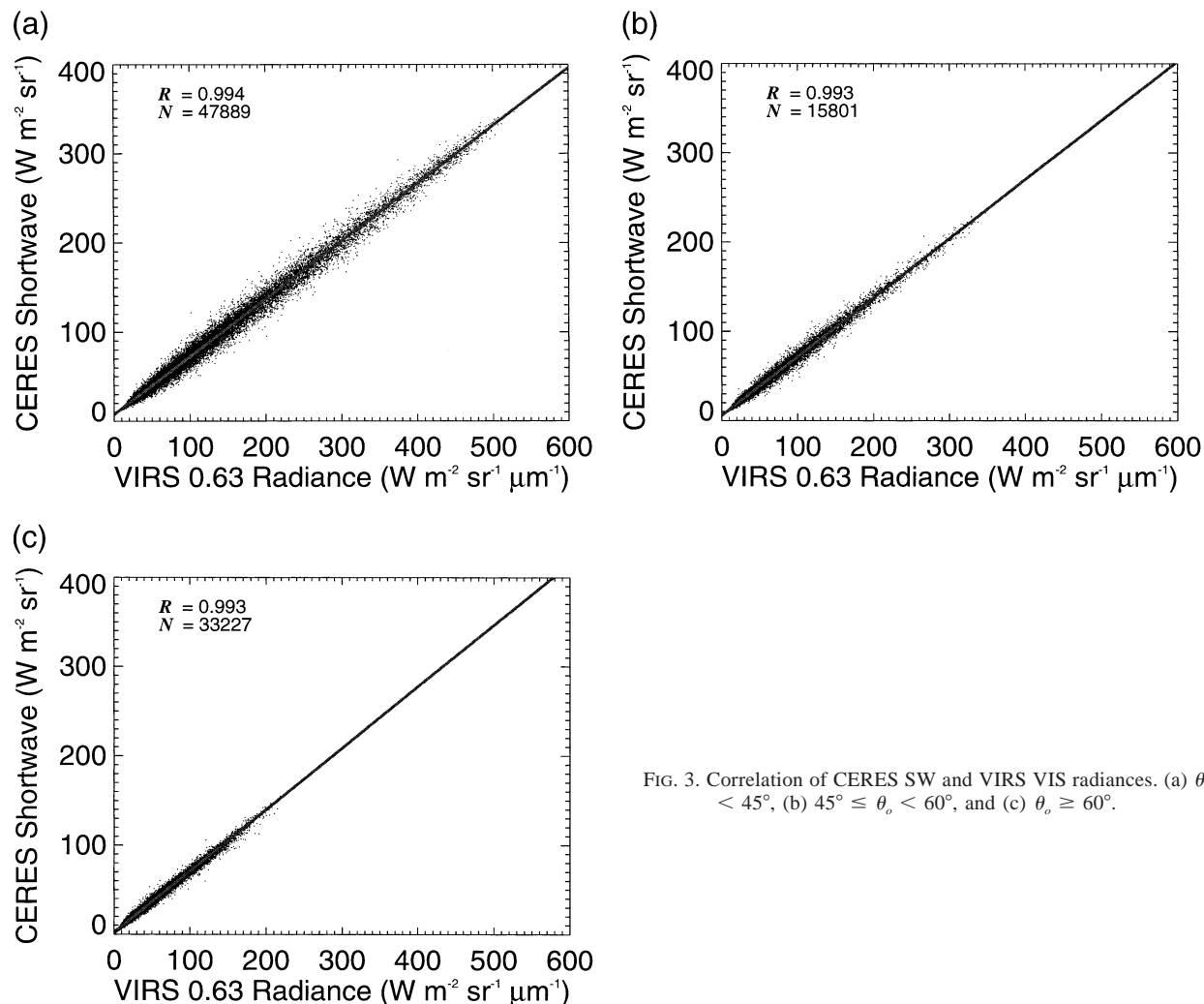


FIG. 3. Correlation of CERES SW and VIRS VIS radiances. (a) $\theta_o < 45^\circ$, (b) $45^\circ \leq \theta_o < 60^\circ$, and (c) $\theta_o \geq 60^\circ$.

two to three times greater. The slopes over desert areas are similar to those over ocean but the intercepts are greater by a factor of 2. The greater intercepts over land and desert arise because the ratio of visible to near-infrared albedo is much greater over land and desert surfaces than over water. Because the spectral distribution of the SW albedo of thick clouds is mostly independent of the surface, the maximum SW and VIS albedos over land and ocean are nearly the same. Thus, the slopes over land and desert are less than those over ocean as compensation for the larger offsets over land. The mean values of R over land and desert are slightly less than those over ocean, but remain above 0.988 in all cases. The ocean trend line for the daily mean slopes in Fig. 4 for SZA between 45° and 60° shows that there is no significant trend in the relationship between the VIS and SW radiances over the first 8 months of VIRS data. Except for a few outliers due to poor sampling, the variation in the daily mean slopes is less than 0.03 in all three SZA bins.

The scatter of the matched VIRS 1.6- μm and CERES

SW data in Fig. 5 is much greater than found for the VIS comparison as reflected in the reduced value of R . Although some of the scatter is likely due to sampling of different climate regimes, sensitivity of the 1.6- μm reflectance to cloud particle phase and size is probably responsible for most of the variation of the SW for a given value of L_{V2} . The broadband reflectance is dominated by conservative scattering as indicated by the tight correlation in Fig. 3. Thus, the thickest ice clouds that produce the greatest SW radiances correspond to lower values of L_{V2} , because the ice crystals in these clouds absorb much of the incoming 1.6- μm radiation. Water clouds yield the greatest values of L_{V2} .

Time series and the corresponding trend lines for the marine SW-NIR gains ($45^\circ < \theta_o < 60^\circ$) in Fig. 6 suggest that the NIR gain may be decreasing by as much as 10% per annum. Table 1 summarizes the apparent degradation rates over ocean for the two channels giving values for the average gain a_m , the mean offset b_m , the computed rate of change in gain Δa , and the initial fitted gain a_o at 1 January 1998. As seen in Fig. 4 and Table

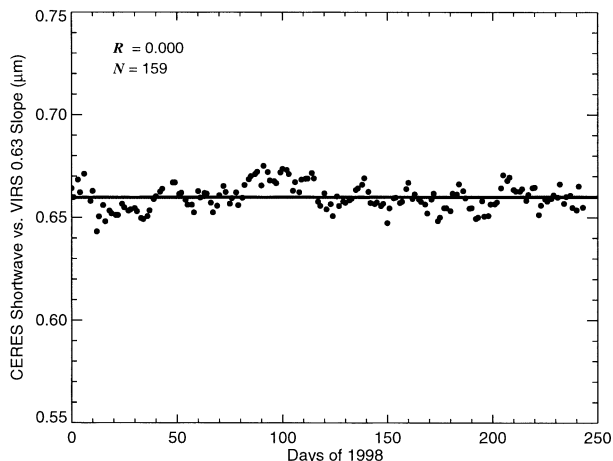


FIG. 4. Time series of daily mean slope in linear fits between CERES SW and VIRS VIS radiances for SZA between 45° and 60°.

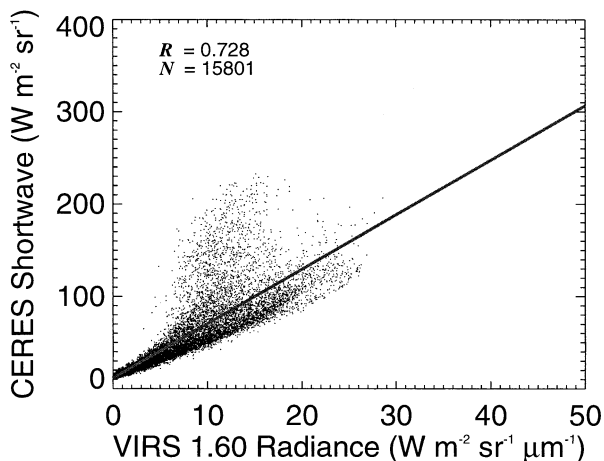


FIG. 5. Correlation of CERES SW and VIRS NIR radiances for SZA between 45° and 60°.

1, the VIS channel relationship is remarkably steady for all SZAs. The mean VIS–SW slopes for land and desert (not listed) also vary with SZA from 0.612 to 0.681 and 0.632 to 0.700, respectively, for the lowest to the highest SZA ranges. The trend lines indicate an average decrease of ~1% per annum in the gain if land and desert scene results are considered. The 1.6- μm results in Table 1 show apparent gain trends over ocean that average approximately $-7\% \text{ yr}^{-1}$. The apparent trends over land and desert are on the same order. Because the 1.6- μm reflectivity is extremely sensitive to cloud phase and particle size as well as vegetation type, the short 8-month record may reflect seasonal changes in these properties.

If seasonal and SZA sampling effects cause the trends seen in Table 1, then the mean slopes taken during the same month in two different years should be similar because similar ranges of SZA are sampled over a given region during the month. Table 2 lists the slopes and offsets for both channels over ocean and for all scene types for channel 1 for March 1998 and 2000. Using the fits for these two months over the full range of observed narrowband values, the SW radiance computed for a given VIS radiance decreases by an average of 0.25% and 0.06% over ocean and land, respectively for the midrange of SZA. The SW radiances computed over ocean from the 1.6- μm fits decreased by an average of 2.2% during the 2 yr. The $1.1\% \text{ yr}^{-1}$ decrease in the near-infrared channel is considerably less than the 10% change found in Fig. 6a indicating that seasonal variations were driving the apparently large degradation rate. All of these differences are within the uncertainties of the fits for the two months of data and, therefore, no statistically significant trends are detected with this approach for any of the VIRS channels, except for the VIRS VIS channel over desert. That trend should be ignored, however, because of the wide variability in desert spectral properties.

Despite some apparent trends in the 8-month datasets, the CERES–VIRS March 1998 and 2000 correlations for each of the VIRS channels suggest that the VIRS calibrations are stable and the VIRS calibration procedures account for any significant degradation in the sensor components. A complete annual cycle of matched data would be more desirable for comparison but it is not available. Narrowband–broadband correlations also do not necessarily constitute an ideal means for assessing the calibration. Their utility depends on how well the quantities are correlated. Certainly, over ocean the surface spectral variations are minimized so that atmospheric conditions are the main source of variability. Figures 3 and 4 demonstrate that the broadband radiances are better suited for assessing the VIS channel than for monitoring the NIR calibration. However, if it is assumed that the conditions sampled over ocean are statistically the same between one time period and another, then highly correlated parameters like all of those

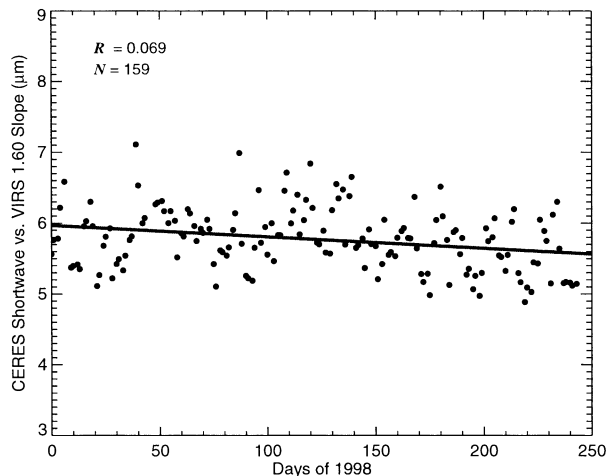


FIG. 6. Time series of daily mean slope in linear fits between CERES SW and VIRS NIR radiances.

TABLE 1. Trends in gain for linear fits between VIRS and CERES radiances over ocean, Jan–Aug 1998.

VIRS–CERES	Condition	a_o (μm)	Δa ($\mu\text{m day}^{-1}$)	a_m (μm)	b_m	R
VIS–SW	$\theta_o < 45^\circ$	0.654	0.02×10^{-4}	0.654	7.47	0.000
	$45 < \theta_o < 60^\circ$	0.660	0.01×10^{-4}	0.660	5.58	0.000
	$\theta_o > 60^\circ$	0.690	0.02×10^{-4}	0.690	2.04	0.000
NIR–SW	$\theta_o < 45^\circ$	6.120	-1.03×10^{-3}	5.996	15.0	0.014
	$45 < \theta_o < 60^\circ$	5.977	-1.68×10^{-3}	5.768	12.6	0.072
	$\theta_o > 60^\circ$	6.343	-1.05×10^{-3}	6.213	4.68	0.025

examined here should yield the same relationship. One means for assessing the differences in Table 2 is to determine if they are beyond the expected variations in the monthly mean slopes. The standard deviations of the differences between the 8-month mean slopes and the monthly mean slopes are 0.8% and 2.9% for the VIS and NIR fits, respectively. All of the differences over ocean surfaces (after averaging SZA-dependent slopes) in Table 2 are within one standard deviation of the month-to-month variability. Using a different approach, Lyu et al. (2000) found that all of the VIRS channel calibrations were stable during the first 11 months of operation. Recently, Lyu (2002, personal communication) used 4 yr of data to conclude that the VIRS VIS channel gain is degrading at an annual rate of 1.15%. Based on these CERES comparisons, however, it is concluded that the onboard systems properly adjusted the VIRS calibrations to account for any sensor degradation throughout the first 27 months of operation and it is concluded that no significant change in the VIRS performance occurred during that period.

5. Visible channel results and discussion

Results from each set of regressions are presented with some discussion. Differences in calibration due to spectral atmospheric effects are computed in the appendix to better understand some of the calibration differences.

a. VIRS versus GOES-8

Figure 7 shows the scatterplots and regression lines for the matched VIS data from *GOES-8* and VIRS taken during February 1998 (Fig. 7a) and 2000 (Fig. 7b). The data are highly correlated with $R \geq 0.990$ and the uncertainties in the slopes for the linear fits are less than 1%. The slope in 2000 is substantially greater than the earlier value, while the space counts differ by only 0.5. The standard error of the estimates using these fits is less than 10%. These results are typical for the other 19 months of matched data. The average space count of 31 derived from the entire matched dataset is slightly greater than the nominal value of 29 (Weinreb et al. 1997). It varies by 3.8% during the period but has no significant trend. Assuming that the space count is a constant value, all of the regression lines were recomputed while forcing the zero radiance through $C_o = 31$.

Figure 8 summarizes the slopes for the entire matched *GOES-8*–VIRS VIS dataset (circles) in the form of a time series with the corresponding trend line (dashed). The latter is referenced to the *GOES-8* launch date, 13 April 1994. The time-dependent slope is

$$g_G = g_G(\text{DSL}) = g_o + \Delta g \text{ DSL}, \quad (9)$$

where DSL is the day since the launch date, g_o is the gain on that date, and the rate of change in gain is Δg . Resulting values for these parameters are given in Table 3. Some scatter is apparent in Fig. 8 indicating that the

TABLE 2. Comparison of CERES broadband radiances to VIRS narrowband radiance regression between Mar 1998 and Mar 2000 for cross-track CERES footprints. All categories had a minimum of 340 000 observations.

Category		Slope (μm)			Intercept		R	
Surface	SZA ($^\circ$)	1998	2000	% diff	1998	2000	1998	2000
SW vs 0.63 μm								
Ocean	0–45	0.654	0.652	–0.21	7.908	7.711	0.997	0.997
	45–60	0.662	0.658	–0.60	5.795	5.967	0.996	0.996
	60–90	0.691	0.690	–0.15	2.101	2.160	0.996	0.996
Land	0–45	0.605	0.602	–0.49	24.16	24.53	0.992	0.992
	45–60	0.621	0.615	–0.97	16.18	16.58	0.992	0.992
	60–90	0.684	0.684	0.00	4.965	4.767	0.988	0.989
Desert	0–45	0.642	0.624	–2.80	14.68	16.29	0.993	0.991
	45–60	0.654	0.633	–3.21	10.45	11.70	0.992	0.993
	60–90	0.713	0.707	–0.84	2.534	2.770	0.994	0.992
SW vs 1.60 μm								
Ocean	0–45	6.080	6.037	–0.71	15.43	13.75	0.812	0.807
	45–60	5.858	5.754	–1.78	13.51	12.36	0.860	0.867
	60–90	6.195	6.218	0.37	5.299	4.405	0.898	0.890

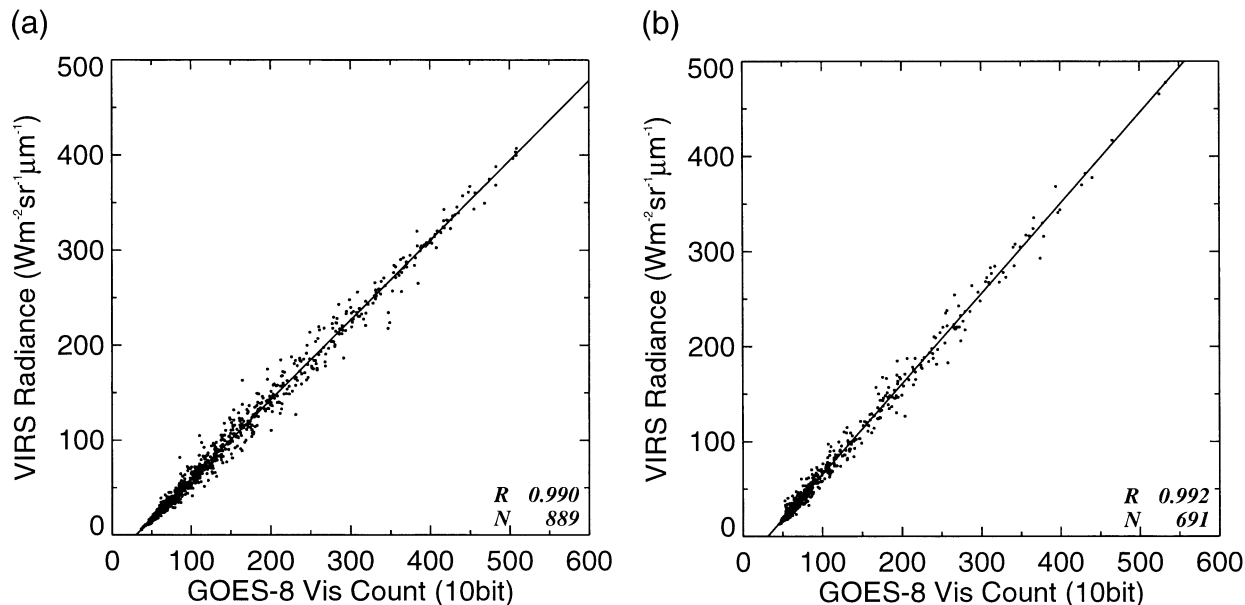


FIG. 7. Correlation of VIRS and GOES-8 VIS data. (a) Feb 1998 and (b) Feb 2000.

single trend line does not exactly reproduce the slopes derived from the regression fits. The rms difference between the observed and trend-line gains in Fig. 8 is 1.2%, a value identical to the rms uncertainty of 1.2% in the individual monthly fits and less than the rms variation of VIRS VIS-channel responsivity measured relative to the sun (Lyu et al. 2000). If a smoothly degrading gain is expected for GOES-8, then it is likely that the derived trend line provides a more accurate representation of the GOES-8 calibration than the instantaneous fits.

b. ATSR-2 versus VIRS

Figure 9 shows the scatterplots of matched VIRS channel-1 and ATSR-2 channel-2 data taken during the

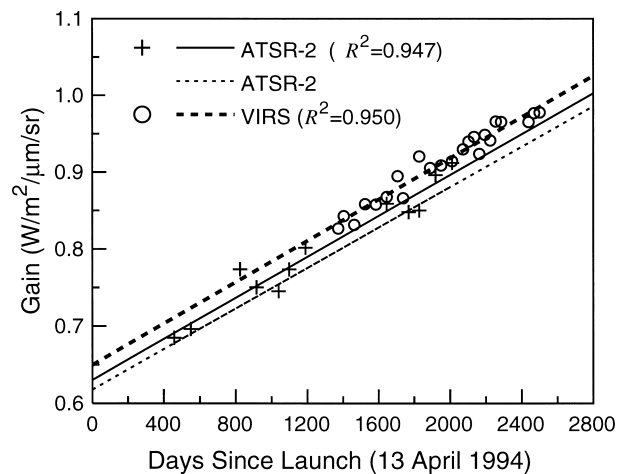


FIG. 8. Time series of GOES-8 VIS gains from VIRS and ATSR-2.

period between February and July 2000. A combination of data from different matched overpasses during the period was needed to obtain enough samples for a reasonable dynamic range and sufficient statistical reliability. The linear fit yields a slope and offset of 1.020 and 0.006, respectively, with $R = 0.990$. The mean difference between the ATSR-2 and VIRS reflectances is -5.5% . A similar analysis using the 1998 matched data yields a slightly different set of coefficients resulting in a smaller mean difference (Table 4). The 1998 dataset contains more points and defines a greater dynamic range than the 2000 dataset.

c. ATSR-2 versus GOES-8

The matched GOES-8 channel-1 and ATSR-2 VIS data taken during October 1995 and the regression fit are shown in Fig. 10. The value of R for this fit is 0.992 indicating an uncertainty of $\sim 1\%$ in the slope of the regression line. Figure 10 is typical of the 12 different GOES-8-ATSR-2 correlations. Coefficients for two of the fits are given in Table 4. The space counts for the ATSR-2-GOES-8 VIS fits vary from 32.4 to 37.3, values that exceed the mean space count derived from the VIRS-GOES-8 regressions. The resulting gains for all of the GOES-8-ATSR-2 VIS correlations (plus signs) are shown in Fig. 8 with the computed trend line (solid). According to the regression fit in Fig. 8, the GOES-8 gain increases by $0.000133 \text{ W m}^{-2} \mu\text{m}^{-1} \text{ sr}^{-1} \text{ day}^{-1}$. The gain on 13 January 1994 is 0.630.

The stability in the VIRS VIS calibration seen in the VIRS-CERES correlations is reinforced by the VIRS-ATSR-2-GOES-8 comparisons. The two lines that fit the GOES-8 data to VIRS and ATSR-2 are nearly par-

TABLE 3. Offsets and trend lines in linear gains geostationary satellite VIS calibrations relative to days since launch for *GOES-8* or days since 1 Jan 1998 for *GMS-5*.

Satellite combination	g_o ($\text{W m}^{-2} \text{sr}^{-1} \mu\text{m}^{-1}$) or c_o	Δg ($\text{W m}^{-2} \text{sr}^{-1} \mu\text{m}^{-1} \text{d}^{-1}$) or Δc (d^{-1})	C_o or ΔT	Std error in $\Delta g\%$
<i>GOES-8-VIRS</i>	0.650	1.341×10^{-4}	31	1.2
<i>GOES-8-ATSR-2</i>	0.630	1.330×10^{-4}	35.5	2.1
<i>GOES-8-ATSR-2*</i>	0.618	1.314×10^{-4}	31	2.2
<i>GMS-5-VIRS</i>	$8.28 \times 10^{-3} \text{ Ct}^{-2}$	$3.13 \times 10^{-7} \text{ Ct}^{-2}$	$-284.3 - 0.632D_{98}$	3.0

* Denotes a forced fit to $c_o = 31$.

allel with a mere 0.8% difference in their slopes. The mean difference in the offsets is 3%, a value smaller than the average difference of 4.4% between the VIRS and ATSR-2 reflectances computed from Table 4. These results suggest that the trend line fit to the VIRS-*GOES-8* data is robust enough for application to data taken anytime after the *GOES-8* became operational.

It is not clear from Fig. 8, however, which imager provides the best accuracy in terms of absolute calibration. In a comparison of the ATSR-2 channel-2 reflectance with the Global Ozone Monitoring Experiment (GOME) spectrometer, Koelemeijer et al. (1998) found that the ATSR-2 reflectance was 2.2% less than collocated, spectrally matched GOME data. Although that difference is approximately half of the difference between the VIRS and ATSR-2 VIS reflectances, it is within the uncertainty of the calibrations of the two instruments. Thus, Koelemeijer et al. (1998) could not determine which instrument was in error. The filter functions (Fig. 2a) of the VIRS and ATSR-2 VIS channels can result in significant differences in the reflectances as shown in the appendix. The differences from the mean of the two VIRS-ATSR-2 fits at $\rho_{A2} = 0.10$ are

nearly identical to the theoretical mean difference as a result of greater Rayleigh scattering in the VIRS spectral band (see appendix). At $\rho_{A2} = 0.57$, however, ρ_{V1} is 0.015 greater than ρ_{A2} , resulting in a difference of 0.032 compared to the theoretical calculations. GOME observations presented by Popp et al. (1997) confirm the theoretical clear sky difference. Thus, part of the average 4.4% difference between VIRS and ATSR-2 is due to the filter functions, but an apparent calibration bias remains and is consistent with the GOME comparison.

The remaining differences between the VIRS and ATSR-2 *GOES-8* fits, however, may be due to the use of the force fit to the *GOES-8* space count. As reported earlier, the *GOES-8* space count determined from the ATSR-2 regressions is between 1 and 6 counts higher than that from VIRS. Similarly, the VIRS-ATSR-2 regression lines do not intersect at (0,0), rather, the reflectance for VIRS averages 0.0094 when the ATSR-2 reflectance is zero. These nonzero offsets are consistent with the range in *GOES-8* space counts determined with ATSR-2 suggesting that the ATSR-2 channel 2 does not measure a true zero radiance. Because of the effects of Rayleigh scattering and the lack of coincident data taken at large SZAs where the radiance would be very small, nonzero offsets are expected. Both *GOES-8* and VIRS should measure greater radiances or reflectances than ATSR-2 at the low end of the range (see appendix) because of more Rayleigh scattering. A linear fit to those data would, therefore, be forced through a nonzero value to accommodate the Rayleigh scattering effect. Given that the relationship between the smaller VIRS and ATSR-2 reflectances agree with theory, it is concluded that ATSR-2 measures a true zero radiance, but it cannot be obtained from linear regression using *GOES-8* and VIRS data. The Rayleigh scattering differences are also the likely explanation for the larger space count derived from VIRS correlations compared to the nominal value. Furthermore, the larger *GOES-8* space counts computed from the ATSR-2 fits compared to those from the VIRS correlations are entirely due to the greater amount of Rayleigh scattering observed by *GOES-8* relative to ATSR-2.

If forced fits are used to compute *GOES-8* gains from the ATSR-2 data, the trend line, shown as the dotted line in Fig. 8, is $0.0001314 \text{ DSL} + 0.618$. In this case,

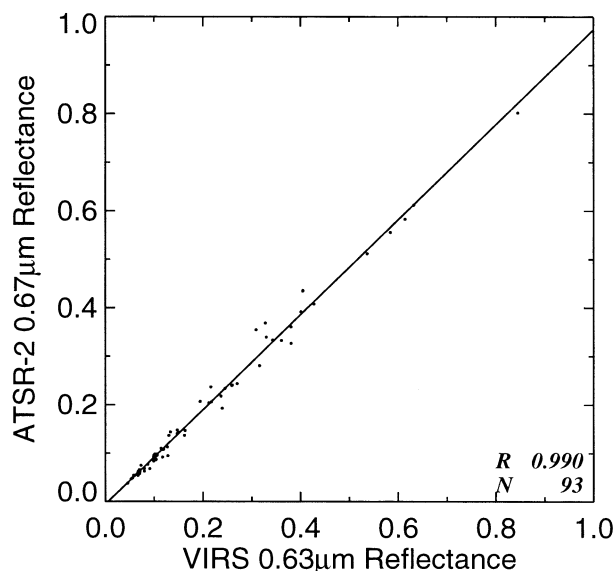


FIG. 9. Correlation of VIRS and ATSR-2 VIS reflectances, Feb-Jul 2000.

TABLE 4. Linear regression and difference statistics for selected VIS-channel correlations.

Spectral band	Date	<i>c</i>	<i>d</i>	$\Delta\rho$ or ΔL (%)
ATSR-2-VIRS	1998	1.001	0.011	3.3
	2000	1.021	0.006	5.5
GOES-8-ATSR-2	Sep 1995	0.685	34.9	7.6
	Oct 1995	0.696	37.1	5.8
VIRS-MODIS	Nov 2000-Mar 2001	0.971	1.66 W m ⁻² sr ⁻¹ μm ⁻¹	8.2

the VIRS and ATSR-2 slopes and offsets differ by only 2% and 4.8%, respectively. This difference in the offsets is closer to the VIRS-ATSR-2 differences. The slope difference remains negligible. After 6 yr, the difference between the ATSR-2 and VIRS-based gains is 4%, a decrease of less than 1% in absolute terms. The coefficients for both trend lines are included in Table 4.

The GOES-8 VIS trend line computed from the VIRS data can be used to estimate the gain at any time during the life of GOES-8 and compared with other estimates of the GOES-8 calibration. Knapp and Vonder Haar (2000) have already performed such comparisons with their trend line, which describes the variation of the calibration coefficient

$$\gamma = 518.2 \text{ W m}^{-2} \text{ sr}^{-1}/m, \quad (10)$$

where *m* is the gain. Fitting the responsivity data from Table 2 of Knapp and Vonder Haar (2000) and converting to gain and normalizing to the solar constant used here yields

$$m = 0.0001525 \text{ DSL} + 0.608. \quad (11)$$

On 1 January 1995, this trend line yields a value of 0.648, which is 5.4% less than the result from VIRS. When DSL = 2000, the gain from (11) is 0.913, a value only 0.5% less than the VIRS-based trend line. The

degradation of the GOES-8 calibration coefficient from the VIRS trend line is 7.5% per year compared to 7.6% from Bremer et al. (1998) and 5.6% estimated by Knapp and Vonder Haar (2000). The latter estimate is referenced to the prelaunch value of $m(\text{DSL} = 0) = 940$ (equivalent slope of $0.561 \text{ W m}^{-2} \text{ sr}^{-1}$) instead of the fit to the line at $\text{DSL} = 0$. If referenced to the fit value of 867 for $\text{DSL} = 0$, the Knapp and Vonder Haar degradation rate is $9.2\% \text{ yr}^{-1}$. The greatest difference occurs at the launch date when the VIRS calibration gives $g_G = 0.650$, which is 6.5% greater than that from (11). This value of g_o in Table 3 is 16% greater than the prelaunch value reported by Weinreb et al. (1997) but is in the range reported by Greenwald et al. (1997) for the initial drop (rise) in the calibration coefficient (gain). The agreement with the results of Bremer et al. (1998) confirms that star-based trending can be valuable for monitoring relative changes in calibration over long periods.

The VIRS fit yields a gain that is 9% greater than that from Minnis and Smith (1998) for April 1996 based on the NOAA-14 Advanced Very High Resolution Radiometer (AVHRR) data, but is very close to that derived by Greenwald et al. (1997) from GOES-9 for late 1995. Li et al. (1998) compared albedos derived from the Scanning Spectral Polarimeter (SSP; Stephens et al. 2000), a well-calibrated airborne radiometer ($\pm 3\text{--}5\%$), and from GOES-8 using with the AVHRR-based calibration reported by Nguyen et al. (1999) and used by Minnis and Smith (1998). The GOES-8 albedos were 0.087 (11.2% relative) less than the SSP albedos from the Li et al. (1998) study. The VIRS calibration for GOES-8 would result in agreement at the 1% level between the SSP and GOES-8 in that October 1995 comparison. Additionally, it would result in much closer agreement between theoretical calculations of broadband albedos in cloudy atmospheres and narrowband-based estimates of broadband shortwave albedo. Finally, use of the VIRS-based current calibration yields cloud optical depths that are in close agreement with those derived from surface radiometers (Dong et al. 2002). From these comparisons, it is concluded that the VIRS-based calibration is more accurate than that derived from the NOAA-14 AVHRR (Nguyen et al. 1999) and should be comparable to the SSP in terms of absolute calibration. Furthermore, given that the GOES-8 VIS channel theoretically should measure reflectances closer to those measured by VIRS than by the ATSR-2 channel 2 be-

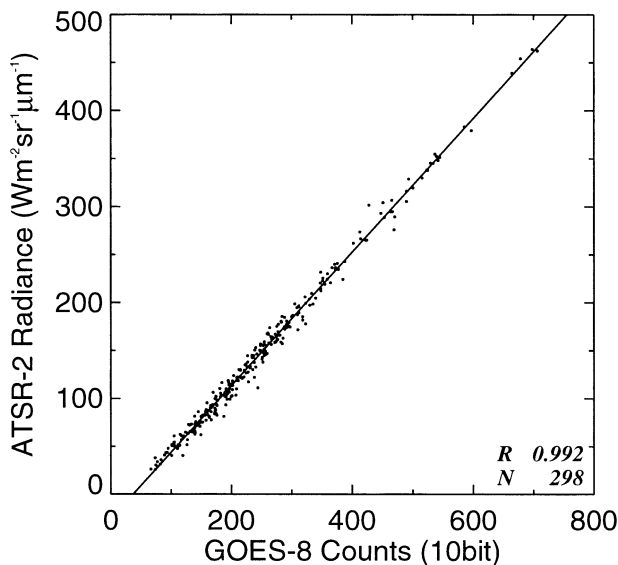


FIG. 10. Correlation of GOES-8 VIS counts and ATSR-2 channel-2 radiance, Oct 1995.

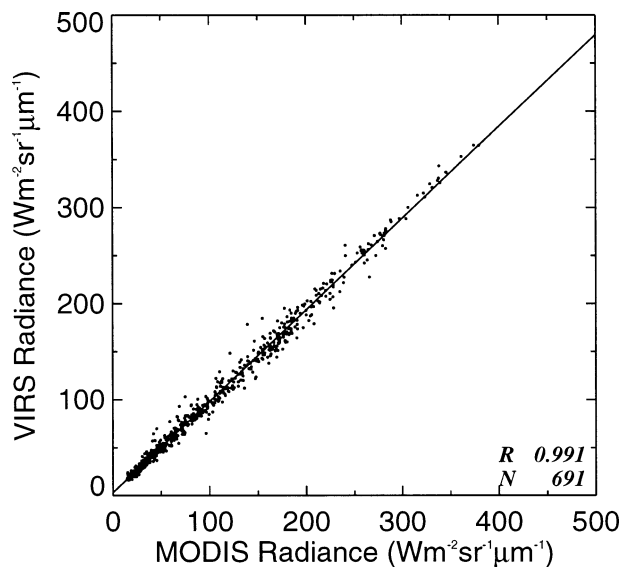


FIG. 11. Correlation of VIRS and MODIS ocean VIS data, Mar 2001.

cause of more similar spectral response characteristics, it is concluded that VIRS should provide a more reliable calibration than ATSR-2 channel 2 for the *GOES-8* VIS channel.

d. MODIS versus VIRS

The scatterplot and linear fit between the March 2001 MODIS and VIRS VIS data in Fig. 11 show a high correlation with a slope of 0.9615 and an offset of 2.01 $\text{W m}^{-2} \text{sr}^{-1} \mu\text{m}^{-1}$. This result is typical of the correlations for the 3 months of data used here. The 3-month

mean slope and offset are listed in Table 4. MODIS and VIRS are equal when $L_{\text{VI}} = 57 \text{ W m}^{-2} \text{sr}^{-1} \mu\text{m}^{-1}$. On average, L_{VI} is 1.5% less than L_{MI} . The VIRS radiances are slightly larger at the darker end of the range while the MODIS values are generally greater at the brighter end. At $300 \text{ W m}^{-2} \text{sr}^{-1} \mu\text{m}^{-1}$, L_{MI} is 2.5% greater than L_{VI} and at $30 \text{ W m}^{-2} \text{sr}^{-1} \mu\text{m}^{-1}$, it is 2.7% less than the VIRS radiance. These differences are consistent in sign with, but are slightly greater than the range of theoretical differences due to Rayleigh scattering and atmospheric absorption (see appendix). Conclusions about statistical differences between the two calibrations should wait for the final MODIS calibrations.

e. VIRS versus GMS-5

Scatterplots and linear fits between the *GMS-5*-squared counts and the VIRS VIS radiances are shown in Fig. 12 for ocean and land for February 2001. The slope difference between the ocean (Fig. 12a) and land (Fig. 12b) fits is small with values of 0.00858 and 0.00873 $\text{W m}^{-2} \text{sr}^{-1} \mu\text{m}^{-1} \text{Ct}^{-2}$, respectively, where Ct represents the counts. However, the land offset, $-1.48 \text{ W m}^{-2} \text{sr}^{-1} \mu\text{m}^{-1}$, is substantially larger than its ocean counterpart, $-5.67 \text{ W m}^{-2} \text{sr}^{-1} \mu\text{m}^{-1}$. Neither offset is positive suggesting that *GMS-5* cannot measure a zero radiance. It is not clear that this is the case, however, because of the strong Rayleigh scattering and weak gaseous absorption in the VIRS band that results in much greater reflectance compared to that for *GMS-5* at small radiances (see appendix). For the 13 months of data between March 2000 and March 2001, the mean slopes are 0.00859 and 0.00891 $\text{W m}^{-2} \text{sr}^{-1} \mu\text{m}^{-1} \text{Ct}^{-2}$ for ocean and land, respectively. The corresponding offsets are -7.58 and $5.69 \text{ W m}^{-2} \text{sr}^{-1} \mu\text{m}^{-1}$. Thus, the ocean

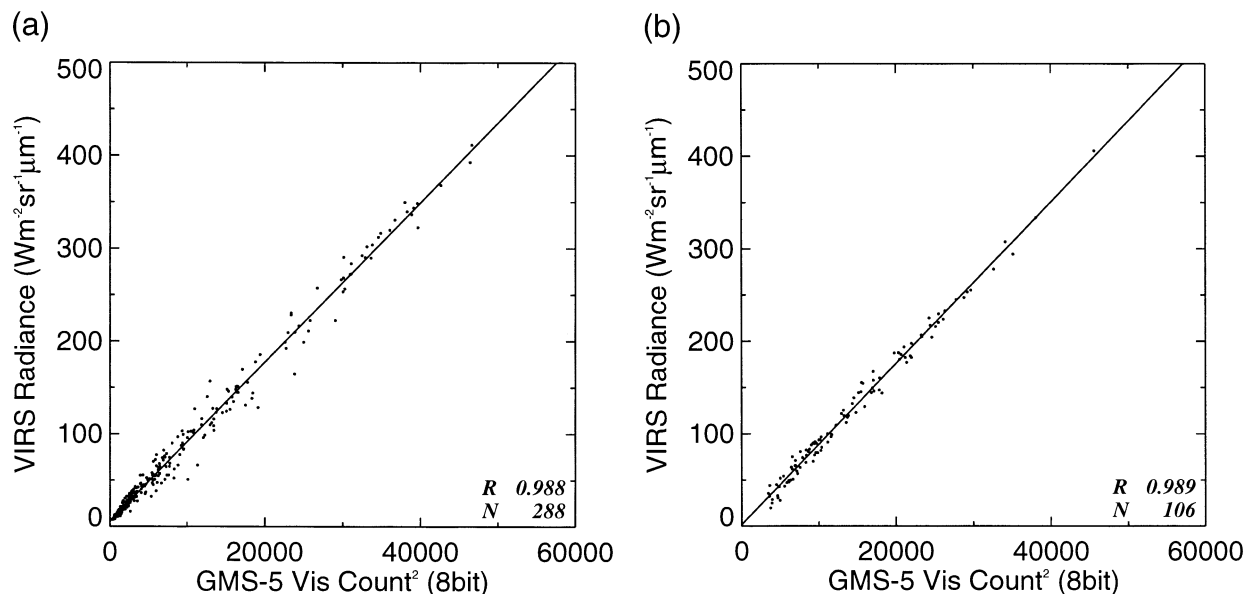


FIG. 12. (a) Correlation of VIRS and *GMS-5* ocean VIS data, Feb 2001 and (b) *GMS-5* land data.

fit for February 2001 is fairly typical while the land fit is somewhat anomalous. The land fits suggest that there is a zero radiance for the *GMS-5* VIS channel. However, close examination of the land plots reveals that the scatter at the dark end is extremely high and the number of data points for each of the ocean results is much greater than for any of the land plots. Thus, it is expected that the ocean results are more reliable. At the high end of the range, the two lines approach each other, differing by only $2.8 \text{ W m}^{-2} \text{ sr}^{-1} \mu\text{m}^{-1}$ at $C_{\text{GM}}^2 = 50\,000$. The respective trend lines for the slope and offset over ocean (Table 3) are

$$g_{\text{GMV}} = 8.276 \times 10^{-3} \text{ W m}^{-2} \text{ sr}^{-1} \mu\text{m}^{-1} \text{ Ct}^{-2} \\ + D_{98} 3.13 \times 10^{-7} \text{ W m}^{-2} \text{ sr}^{-1} \mu\text{m}^{-1} \text{ Ct}^{-2} \text{ day}^{-1}, \quad (12)$$

and

$$C_{\text{GMo}}^2 = -248.3 - 0.6322D_{98}, \quad (13)$$

where D_{98} is the number of days since 1 January 1998. The land trends are not statistically significant.

The *GMS-5* VIS calibration slopes varied with a standard deviation of 3.6% and 5.6% over ocean and land, respectively. Some of the difference in the variability is due to the number of samples. All of the ocean fits used, at least, 170 points, while many of the land calibrations used fewer than 50 points. Additional differences arise because of the wide variability in near-infrared spectral reflectance with land surface type. Deserts and grasslands in Australia will have very different spectral characteristics over the *GMS-5* filter function than tropical forests. Nonuniform sampling of these different surfaces from month to month will cause some variations in the slope. The difference between the ocean and land mean calibration coefficients is primarily due to this spectral difference. Water bodies have spectrally flat albedos across the *GMS-5* spectrum while most land surfaces are relatively dark for wavelengths, $\lambda < 0.7 \mu\text{m}$, but much brighter at longer wavelengths. Thus, most of the signal for the land surfaces comes from the near-infrared spectrum resulting in the large differences in the ocean and land offsets.

These results highlight the importance of properly characterizing the surface spectrally when interpreting a calibration using a channel with no near-infrared wavelengths. The International Satellite Cloud Climatology Project currently uses a similar VIS channel on the AVHRR for intercalibrating all of its satellites including the *GMS* and *Meteosat* series, which carry broadband VIS imagers (Desormeaux et al. 1993). Only a single calibration is used for normalizing the AVHRR and *GMS* in the *GMS* calibration. Use of the ocean fit for the land radiance may cause some biases in products derived from the broadband *GMS* or *Meteosat* sensors. The spectral differences may also affect the use of the ocean-based calibration for applications to *GOES-8* data over land, but to a lesser extent than for *GMS* or *Me-*

teosat. It is not clear how the single calibration approach will affect the derived cloud properties and, therefore, additional study of the spectral effect is needed.

Le Marshall et al. (1999) performed a calibration of the *GMS-5* using near-nadir matched *NOAA-14* AVHRR data for data taken between February 1996 and June 1997. Their approach, using only cloudy targets, related AVHRR channel-1 (VIS) 10-bit counts to C_{GM}^2 . The resulting average slope and offset are 0.0128 C^{-1} and 41.2 , respectively. Subtracting the AVHRR space count of 41 and dividing by their AVHRR responsivity of $0.617 \text{ W m}^{-2} \mu\text{m}^{-1} \text{ sr}^{-1} \text{ Ct}^{-1}$ and normalizing the AVHRR solar constant of $510.9 \text{ W m}^{-2} \mu\text{m}^{-1} \text{ sr}^{-1}$ to that used here yields $L_{\text{GM1}} = 0.008138 \text{ W m}^{-2} \mu\text{m}^{-1} \text{ sr}^{-1} \text{ Ct}^{-2}$. This gain is only 5.6% less than the value derived here using *VIRS*. If the *VIRS*-derived slope is computed for 15 November 1996, the midpoint of the Le Marshall et al. (1999) dataset, the resulting slope is $0.008147 \text{ W m}^{-2} \mu\text{m}^{-1} \text{ sr}^{-1} \text{ Ct}^{-2}$ with a squared offset count of 11. The agreement in both slope and intercept between the two methods is well within the uncertainty bounds of Le Marshall et al. (1999) results. This result confirms the slow degradation of 1.3% per year in the *GMS-5* VIS channel gain and consistency between the *VIRS* calibration and the AVHRR responsivity used by Le Marshall et al. (1999).

6. Conclusions

Consistent long-term calibrations of satellite imagers are essential for monitoring changes in the climate system from space. Onboard calibration systems, generally applied only to infrared channels on operational meteorological satellites, can be valuable for maintaining the calibration stability of solar channels on other satellites. This stability has been confirmed for both the *VIRS* and *ATSR-2* solar channels by comparisons with well-characterized broadband measurements from *CERES* and from trend lines derived from comparisons with narrowband *GOES-8* data for overlapping times during a 6-yr period. Most of the mean differences between the measurements from the various sensors can be attributed to the spectral filter functions, which are unique to a given instrument. Much of the random error is due to the angle and time differences between matched measurements. It is clear that the larger spectral differences between narrow- and broadband instruments require a much longer time and space sample of matched data, relative to data from similar spectral bands, if the latter is to provide a reference for detecting trends in the calibration of the former.

It is concluded that the *VIRS* is more appropriate than *ATSR-2* as a calibration reference for the *GOES-8* VIS channel. The *VIRS* VIS channel is more similar to the *GOES-8* spectrum and the *ATSR-2* may underestimate reflectance for bright scenes. Use of the *VIRS* to develop a calibration trend for *GMS-5* results in excellent agreement with a previous intercalibration that was based on

an independent technique. Optical depths computed using the *GOES-8* VIRS calibrations are, on average, 4.5% less than coincident surface-based estimates. Use of the ATSR-2 calibration would result in a greater underestimate of the optical depth. However, an assessment of the VIRS absolute accuracy is still needed.

Traditionally, various VIS imagers have been intercalibrated directly without concern for spectral differences in the imager filter functions. It has been clearly demonstrated that even small differences in spectral filter functions for VIS channels should cause differences of a few percent in reflectances measured by two perfectly calibrated instruments viewing the same scene due to variations in Rayleigh scattering and atmospheric absorption. Such differences may be important in the retrievals of cloud properties and surface albedos from two such sensors because they may cause some biases in the results. Thus, when attempting to derive consistent datasets from two or more imagers, it may be necessary to force the intercalibrations to match the expected theoretical relationships between the reflectances that would be measured by the relevant instruments. Such forced calibrations may require the use of nonlinear regressions or sets of linear regression. In the meantime, it is important to understand the magnitude and impact of the spectral differences on the intercalibrations performed in the traditional manner.

This study has demonstrated that the VIRS VIS channel, as one of several sensors with onboard calibration, can serve as a reliable reference for calibrating other satellites. If the agreement between the VIRS and MODIS VIS channels in the preliminary assessment remains when the final MODIS data are released, then the MODIS VIS channel could be used as a reference instead of VIRS. Additionally, with some corrections for the bias between VIRS and ATSR-2, the latter could also serve as a reference because of its apparent long-term stability. With a reliable trend line developed from intercalibrations with such references, it is possible to transfer the calibration of one meteorological satellite to others in near real time as discussed in Part III of this paper.

Acknowledgments. This research was supported by the CERES Project through the NASA Earth Science Enterprise and by the Environmental Sciences Division of U.S. Department of Energy Interagency Agreement DE-AI02-97ER62341 through the ARM Program. The ATSR-2 data were provided by the ATSR Data Processing Laboratory, Rutherford Appleton Laboratory, Chilton, United Kingdom, with the assistance of Mr. Nigel Houghton under the sponsorship of the Natural Environment Research Council and the European Space Agency. Thanks to Vince Salomonson and William Barnes of the MODIS team for their assistance with the MODIS data and the NASA Langley Distributed Active Archive Center for supplying the CERES, MODIS, and VIRS data. The *GOES-8* and *GMS-5* data were acquired from the University of Wisconsin Space Science and

Engineering Center. The Rayleigh scattering simulations were provided by Robert Arduini of SAIC in Hampton, Virginia. Thanks to Douglas Spangenberg for this helpful comments.

APPENDIX

Atmospheric and Surface Reflectance Effects

A complete treatment of the detailed effects of the surface and atmosphere on reflectance in the spectral bands defined by the imager filter functions is beyond the scope of this paper. However, it is important to at least consider some of the main variables affecting the reflectances in the VIS wavelengths to better understand differences in the calibrations. The specific cases discussed below are meant to give the extreme effects due to Rayleigh scattering and gaseous absorption. Actual realizations should produce differences somewhere within the range defined by these theoretical extremes. Aerosol scattering and absorption and surface spectral reflectance are not considered, but should be when intercalibrations are performed over land or hazy ocean surfaces.

a. Rayleigh scattering and atmospheric absorption calculations

Besides aerosols, Rayleigh scattering and gaseous absorption are the most variable processes attenuating the radiation at VIS wavelengths. Spectral surface reflectance is also highly variable for a given land scene but should be relatively uniform for deep oceans. To examine the impact of Rayleigh scattering, Rayleigh optical depths were computed for each imager by convolving the spectral Rayleigh optical depth for a given atmospheric thickness with the spectral solar constant over the filter function of each instrument. These integrated Rayleigh optical depths were then used in an adding-doubling radiative transfer program to compute TOA reflectances and radiances for each imager over a surface with albedos of 0.04 and 0.24 at $\mu_o = 0.95, 0.75, \text{ and } 0.55$; $\theta = 25.8^\circ \text{ and } 45.6^\circ$; $\phi = 5^\circ, 30^\circ, 60^\circ, 90^\circ, 120^\circ, 150^\circ, \text{ and } 175^\circ$. The computations were performed using cloud optical depths of 0.5, 2, 8, 32, and 128 for water droplet clouds at 900 hPa with an effective droplet radius of 12 μm and ice crystal clouds with an effective diameter of 24 μm at 200 hPa (Minnis et al. 1998). The radiances were also computed for the *NOAA-14* AVHRR channel 1 for future reference. Linear regression was applied to the results to simulate the intercalibrations for each pair of imagers. The resulting linear coefficients are given in Table A1 along with the Rayleigh optical depths τ_R for a 1013-hPa atmosphere. The Rayleigh optical depths vary by almost a factor of two for the considered imagers.

For simplicity, the atmospheric absorption effects were considered separately. Combined up and down atmospheric transmission was computed with a correlated

TABLE A1. Theoretical linear regression coefficients for VIS channels considering Rayleigh scattering. Rayleigh optical depths at 1013 hPa are given in brackets.

y (imager)	x (imager)	a	b (W m ⁻² sr ⁻¹ μm ⁻¹)
VIRS [0.0566]	GOES-8 [0.0613]	1.0044	-1.39
VIRS	ATSR-2 [0.0448]	1.0050	-1.65
VIRS (reflectance)	ATSR-2 (reflectance)	0.9789	0.0139*
ATSR-2	GOES-8	1.0095	-3.04
VIRS	MODIS [0.0485]	0.9973	0.89
VIRS	GMS-5 [0.0314]	0.9875	0.395
VIRS	NOAA-14 AVHRR [0.0492]	0.9998	0.12

* No units associated with the coefficient.

k-distribution method for each imager at $\theta_o = 53.13^\circ$ and $\theta = 53.13^\circ$ for three standard atmospheric profiles, tropical (TR), midlatitude winter, and sub-Arctic winter (SAW), to determine the sensitivity to changes in ozone and water vapor. The correlated *k*-distribution coefficients were computed as in Kratz (1995) for the ATSR-2, GOES-8, MODIS, and GMS-5 channels. (These coefficients are available online at <http://asd-www.larc.nasa.gov/~kratz/>.) The primary absorbers in the VIS region are water vapor and ozone. These two gases, as well as all other known significant absorbing gases, were used in formulating the coefficients. The resulting atmospheric transmittances are listed in Table A2. On average, ozone only accounts for about half of the absorption for a TR atmosphere, but contributes more than 75% of the absorption for the SAW where water vapor is scarce.

b. VIRS–GOES-8–ATSR-2

The Rayleigh calculations indicate that the GOES-8 radiance should be approximately 1.2 W m⁻² sr⁻¹ or 3% greater than the VIRS value for $L_G = 35 \text{ W m}^{-2} \text{ sr}^{-1} \mu\text{m}^{-1}$, while the two values should be nearly identical for $L_G = 350 \text{ W m}^{-2} \text{ sr}^{-1} \mu\text{m}^{-1}$. The greater GOES-8 τ_R has more impact for dark scenes and minimal effect for brighter scenes. Even for the most extreme atmospheric absorption in the Tropics (Table A2), the difference at $35 \text{ W m}^{-2} \text{ sr}^{-1} \mu\text{m}^{-1}$ would only be reduced by 2%. Because the calibrations are performed directly with GOES counts, it is not possible to determine whether the observations are consistent with the theoretical calculations for GOES-8 and VIRS.

TABLE A2. Gaseous atmospheric transmission for VIS channels for standard atmospheric profiles at $\theta_o = 53.13^\circ$ and $\theta = 53.13^\circ$. Percent contribution to total absorption by ozone is given in parentheses.

Imager	Sub-Arctic winter	Midlatitude winter	Tropical
VIRS	0.9216 (91)	0.9314 (86)	0.9398 (61)
GOES-8	0.9279 (71)	0.9318 (63)	0.9234 (35)
ATSR-2	0.9520 (91)	0.9555 (55)	0.9441 (41)
MODIS	0.9407 (93)	0.9480 (89)	0.9520 (60)
GMS-5	0.9379 (52)	0.9323 (40)	0.8995 (17)
AVHRR	0.9304 (80)	0.9334 (70)	0.9170 (35)

The ATSR-2 and VIRS data provide a more direct comparison with theory. Considering only the greater VIRS τ_R , VIRS should measure larger reflectances than ATSR-2 at low values while the two reflectances should be nearly equal at larger reflectances. Assuming clear skies, the average VIRS reflectance for the SAW and TR atmospheres should be 0.0093 greater than the ATSR-2 value when $\rho_{A2} = 0.10$. However, when ρ_{A2} is 0.57 for a cloudy atmosphere using the SAW to simulate the dry cold air above a high cloud, ρ_{V1} would be 0.017 less than ρ_{A2} . Thus, VIRS would be expected to measure larger radiances than ATSR-2 for most clear areas but would observe smaller radiances for cloudy or snow-covered scenes.

The value of τ_R for GOES-8 is nearly 0.02 larger than the ATSR-2 value while the GOES-8 absorption is greater than the ATSR-2 absorption. Thus, for $L_{A2} = 30.5 \text{ W m}^{-2} \text{ sr}^{-1} \mu\text{m}^{-1}$ in a clear TR atmosphere, $L_G = \text{W m}^{-2} \text{ sr}^{-1} \mu\text{m}^{-1}$, a value that can be compared to $L_{V1} = 31.5 \text{ W m}^{-2} \text{ sr}^{-1} \mu\text{m}^{-1}$. Using a cloud below an SAW atmosphere and $L_{A2} = 333.5 \text{ W m}^{-2} \text{ sr}^{-1} \mu\text{m}^{-1}$, $L_G = 324.8 \text{ W m}^{-2} \text{ sr}^{-1} \mu\text{m}^{-1}$. Thus, for perfect calibrations, GOES-8 should yield larger radiances than either VIRS or ATSR-2 when the radiance is small, but it should observe smaller radiances than ATSR-2 for bright cloudy scenes.

c. VIRS–MODIS

The VIRS Rayleigh optical depth is 17% greater than the MODIS value resulting in larger reflectances at small radiance values. For the TR atmosphere with $L_{M1} = 33.2 \text{ W m}^{-2} \text{ sr}^{-1} \mu\text{m}^{-1}$, $L_{V1} = 33.6 \text{ W m}^{-2} \text{ sr}^{-1} \mu\text{m}^{-1}$, a difference of 1%. For bright cloudy scenes, the smaller absorption for MODIS channel 1 yields larger radiances than VIRS. Using the SAW atmosphere and $L_{V1} = 322.5 \text{ W m}^{-2} \text{ sr}^{-1} \mu\text{m}^{-1}$, $L_{M1} = 329.2 \text{ W m}^{-2} \text{ sr}^{-1} \mu\text{m}^{-1}$, a difference of -2%. Thus, MODIS should observe larger radiances than VIRS for bright cloudy scenes and slightly smaller values for dim scenes.

d. VIRS–GMS-5 and VIRS–AVHRR

Rayleigh scattering is the least for GMS-5 with τ_R nearly half the value of its VIRS counterpart. In addi-

tion, the absorption in the TR atmosphere is considerably greater than that for VIRS. Using the regression fits and a TR atmosphere for a clear scene, $L_{V1} = 37.5 \text{ W m}^{-2} \text{ sr}^{-1} \mu\text{m}^{-1}$ when $L_{GM} = 31.5 \text{ W m}^{-2} \text{ sr}^{-1} \mu\text{m}^{-1}$. Using the SAW atmosphere for a bright scene yields $L_{V1} = 322.2 \text{ W m}^{-2} \text{ sr}^{-1} \mu\text{m}^{-1}$ when $L_{GM} = 328.3 \text{ W m}^{-2} \text{ sr}^{-1} \mu\text{m}^{-1}$. Thus, VIRS is likely to measure smaller radiances than GMS-5 for bright scenes. For the same set of conditions, $L_{V1} = 33.0$ and $322.7 \text{ W m}^{-2} \text{ sr}^{-1} \mu\text{m}^{-1}$, when the corresponding NOAA-14 AVHRR radiances are 32.1 and $325.6 \text{ W m}^{-2} \text{ sr}^{-1} \mu\text{m}^{-1}$, respectively.

REFERENCES

- Abel, P., B. Guenther, R. N. Gallimore, and J. W. Cooper, 1993: Calibration results for NOAA-11 AVHRR channels 1 and 2 from congruent path aircraft observations. *J. Atmos. Oceanic Technol.*, **10**, 493–508.
- Barkstrom, B. R., E. F. Harrison, and R. B. Lee III, 1990: Earth Radiation Budget Experiment—Preliminary seasonal results. *Eos*, **71**, 297 and 304.
- Barnes, R. A., W. L. Barnes, C.-H. Lyu, and J. L. Gales, 2000: An overview of the Visible and Infrared Scanner radiometric calibration algorithm. *J. Atmos. Oceanic Technol.*, **17**, 395–405.
- Barnes, W. L., T. S. Pagano, and V. V. Salomonson, 1998: Pre-launch characteristics of the Moderate Resolution Imaging Spectroradiometer (MODIS) on EOS-AM1. *IEEE Trans. Geosci. Remote Sens.*, **36**, 1088–1100.
- Bremer, J. C., J. G. Baucom, H. Vu, M. P. Weinreb, and N. Pinkine, 1998: Estimation of long-term throughput degradation of GOES 8 & 9 visible channels by statistical analysis of star measurements. *Proc. SPIE Conf. on Earth Observing Systems III*, San Diego, CA, SPIE, 145–154.
- Butler, J. J., and R. A. Barnes, 1998: Calibration strategy for the earth observing system (EOS)-AM1 platform. *IEEE Trans. Geosci. Remote Sens.*, **36**, 1056–1061.
- Desormeaux, Y., W. B. Rossow, C. L. Brest, and G. G. Campbell, 1993: Normalization and calibration of geostationary satellite radiances for ISCCP. *J. Atmos. Oceanic Technol.*, **10**, 304–325.
- Doelling, D. R., P. Minnis, D. A. Spangenberg, V. Chakrapani, A. Mahesh, F. P. J. Valero, and S. Pope, 2001: Cloud radiative forcing during FIRE ACE derived from AVHRR data. *J. Geophys. Res.*, **106**, 15 279–15 296.
- Dong, X., P. Minnis, G. G. Mace, W. L. Smith Jr., M. Poellot, and R. Marchand, 2002: Comparison of stratus cloud properties deduced from surface, GOES, and aircraft data during the March 2000 ARM Cloud IOP. *J. Atmos. Sci.*, in press.
- Green, R. N., and B. A. Wielicki, 1995: Convolution of imager cloud properties with CERES footprint point spread function (subsystem 4.4). Clouds and the Earth's Radiant Energy System (CERES) algorithm theoretical basis document, Vol. 3, Cloud analyses and radiance inversions (subsystem 4). NASA Rep. 1376, 177–194.
- Greenwald, T. J., S. A. Christopher, and J. Chou, 1997: Cloud liquid water path comparisons from passive microwave and solar reflectance satellite measurements: Assessment of sub-field-of-view cloud effects in microwave retrievals. *J. Geophys. Res.*, **102**, 19 585–19 596.
- Iqbal, M., 1983: *An Introduction to Solar Radiation*. Academic Press, 390 pp.
- Knapp, K. R., and T. H. Vonder Haar, 2000: Calibration of the eighth Geostationary Observational Environmental Satellite (GOES-8) imager visible sensor. *J. Atmos. Oceanic Technol.*, **17**, 1639–1642.
- Koelemeijer, R. B. A., P. Stammes, and P. D. Watts, 1998: Comparison of visible calibrations of GOME and ATSR-2. *Remote Sens. Environ.*, **63**, 279–288.
- Kratz, D. P., 1995: The correlated k -distribution technique as applied to the AVHRR channels. *J. Quant. Spectrosc. Radiat. Transfer*, **53**, 501–517.
- Kriebel, K. T., and V. Amann, 1993: Vicarious calibration of the Meteosat visible. *J. Atmos. Oceanic Technol.*, **10**, 225–232.
- Li, Z., A. Trischchenko, H. W. Barker, G. L. Stephens, P. Partain, and P. Minnis, 1998: Consistency analyses of ARESE measurements for studying cloud absorption. *Proc. Eighth Annual ARM Science Team Meeting*, Tuscon, AZ, ARM, 417–421.
- Lee, R. B., III, and Coauthors, 1998: Pre-launch calibrations of the Clouds and Earth's Radiant Energy System (CERES) Tropical Rainfall Measuring Mission and Earth Observing System Morning (EOS-AM1) spacecraft thermistor bolometer sensors. *IEEE Trans. Geosci. Remote Sens.*, **36**, 1173–1185.
- Le Marshall, J. F., J. J. Simpson, and Z. Jin, 1999: Satellite calibration using a collocated nadir observation technique: Theoretical basis and application to the GMS-5 pathfinder benchmark period. *IEEE Trans. Geosci. Remote Sens.*, **37**, 499–507.
- Lyu, C. H., R. A. Barnes, and W. L. Barnes, 2000: First results from the on-orbit calibrations of the Visible and Infrared Scanner for the Tropical Rainfall Measuring Mission. *J. Atmos. Oceanic Technol.*, **17**, 385–394.
- Menzel, W. P., and J. F. W. Purdom, 1994: Introducing GOES-I: The first of a new generation of Geostationary Operational Environmental Satellites. *Bull. Amer. Meteor. Soc.*, **75**, 757–781.
- Minnis, P., and E. F. Harrison, 1984: Diurnal variability of regional cloud and clear-sky radiative parameters derived from GOES data. Part III: November 1978 radiative parameters. *J. Climate Appl. Meteor.*, **23**, 1032–1052.
- , and W. L. Smith Jr., 1998: Cloud and radiative fields derived from GOES-8 during SUCCESS and the ARM-UAV spring 1996 flight series. *Geophys. Res. Lett.*, **25**, 1113–1116.
- , —, D. P. Garber, J. K. Ayers, and D. R. Doelling, 1995: Cloud properties derived from GOES-7 for the Spring 1994 ARM Intensive Observing Period using version 1.0.0 of the ARM satellite data analysis program. NASA Rep. 1366, 59 pp.
- , D. P. Garber, D. F. Young, R. F. Arduini, and Y. Takano, 1998: Parameterization of reflectance and effective emittance for satellite remote sensing of cloud properties. *J. Atmos. Sci.*, **55**, 3313–3339.
- , L. Nguyen, D. R. Doelling, D. F. Young, and D. P. Kratz, 2002: Rapid calibration of operational and research meteorological satellite imagers. Part II: Comparison of infrared channels. *J. Atmos. Oceanic Technol.*, **19**, 1250–1266.
- Mutlow, C. T., M. J. Murray, D. L. Smith, P. D. Watts, and P. North, 1999: New data sets for climate change and land use studies are on track. *Eos*, **49**, 589 and 594.
- Nguyen, L., P. Minnis, J. K. Ayers, W. L. Smith Jr., and S. P. Ho, 1999: Intercalibration of geostationary and polar satellite data using AVHRR, VIRS, and ATSR-2 data. *Proc. 10th Conf. on Atmospheric Radiation*, Madison, WI, Amer. Meteor. Soc., 405–408.
- Popp, T., G. Gesell, T. König, T. Kriebel, R. Meerkötter, and H. Mannstein, 1997: Exploiting GOME and ATSR-2 data: First results of the PAGODA Project. *Third ERS Symp.*, Florence, Italy, European Space Agency. [Available online at <http://earth.esa.int/symposia/papers/popp>.]
- Priestley, K. J., and Coauthors, 2000: Postlaunch radiometric validation of the Clouds and the Earth's Radiant Energy System (CERES) proto-flight model on the Tropical Rainfall Measuring Mission (TRMM) spacecraft through 1999. *J. Appl. Meteor.*, **39**, 2249–2258.
- Rao, C. R. N., and J. Chen, 1996: Post-launch calibration of the visible and near-infrared channels of the Advanced Very High Resolution Radiometer on NOAA-14 spacecraft. *Int. J. Remote Sens.*, **17**, 2743–2747.

- Slater, P. N., S. F. Biggar, K. J. Thome, D. I. Gellman, and P. R. Spyak, 1996: Vicarious radiometric calibration of EOS sensors. *J. Atmos. Oceanic Technol.*, **13**, 349–358.
- Smith, D. L., P. D. Read, and C. T. Mutlow, 1997: The calibration of the visible/near infra-red channels of the Along-Track Scanning Radiometer-2 (ATSR-2). *Sensors, Systems and Next-Generation Satellites*, H. Fujisadsa, Ed., Proceedings of SPIE, Vol. 3221, International Society for Optical Engineering, 53–62.
- Stephens, G. L., R. F. McCoy Jr., R. B. McCoy, P. Gabriel, P. T. Partain, and S. D. Miller, 2000: A multipurpose Scanning Spectral Polarimeter (SSP): Instrument description and sample results. *J. Atmos. Oceanic Technol.*, **17**, 616–627.
- Thomas, S., and Coauthors, 2000: On-orbit radiometric performance results of CERES instruments aboard Tropical Rainfall Measuring Mission (TRMM) and Earth Science Enterprise Terra spacecraft. *Proc. Fifth Pacific Ocean Remote Sensing Conf.*, Goa, India, Australian Bureau of Meteorology, 127–131.
- Trishchenko, A., and Z. Li, 1998: Use of ScaRaB measurements for validating a GOES-based TOA radiation product. *J. Appl. Meteor.*, **37**, 591–605.
- Weinreb, M., M. Jamison, N. Fulton, Y. Chen, J. X. Johnson, J. Brenner, C. Smith, and J. Baucom, 1997: Operational calibration of Geostationary Operational Environmental Satellite-8 and -9 imagers and sounders. *Appl. Opt.*, **36**, 6895–6904.
- Whitlock, C. H., S. R. LeCroy, and R. J. Wheeler, 1994: SRB/FIRE satellite calibration results and their impact on ISCCP. *Proc. Eighth Conf. on Atmospheric Radiation*, Nashville, TN, Amer. Meteor. Soc., 52–54.
- Wielicki, B. A., and Coauthors, 1998: Clouds and the Earth's Radiant Energy System (CERES): Algorithm overview. *IEEE Trans. Geosci. Remote Sens.*, **36**, 1127–1141.